Universal Map for Fractal Structures in Weak Interactions of Solitary Waves

Yi Zhu,[1] Richard Haberman,[2] and Jianke Yang[3]

[1]*Zhou Pei-Yuan Center for Applied Mathematics, Tsinghua University, Beijing 100084, China*
[2]*Department of Mathematics, Southern Methodist University, Dallas, Texas 75275, USA*
[3]*Department of Mathematics and Statistics, University of Vermont, Burlington, Vermont 05401, USA*

Fractal scatterings in weak solitary-wave interactions are analyzed for generalized nonlinear Schrödiger equations (GNLS). Using asymptotic methods, these weak interactions are reduced to a universal second-order map. This map gives the same fractal-scattering patterns as those in the GNLS equations both qualitatively and quantitatively. Scaling laws of these fractals are also derived.

PACS numbers: 42.65.Tg, 05.45.Yv, 42.81.Dp

Solitary-wave interactions are fascinating mathematical phenomena, and they arise in numerous physical applications such as water waves and nonlinear optics [1–3]. Strong interactions occur when two solitary waves are initially far apart but move toward each other at moderate or high speeds. Weak interactions would occur if the two waves are initially well separated, and their relative velocities are small. In integrable wave equations, strong interactions of solitary waves are elastic, and their weak interactions exhibit interesting but simple dynamics [1,2,4]. In nonintegrable systems, however, solitary-wave interactions can be extremely complicated. Indeed, one of the most important developments in the nonlinear wave theory in recent years is the discovery of fractal scatterings of solitary-wave interactions in nonintegrable equations [5–11]. On the analysis of fractal scatterings, some progress has been made. For strong interactions, various collective-coordinate ordinary differential equations (ODEs) based on qualitative variational methods have been derived and analyzed [6–8,11]. From the variational ODEs, a separatrix map was derived, showing chaotic scatterings [11]. On weak interactions, a simple asymptotically accurate ODE model was derived for the generalized nonlinear Schrödinger (NLS) equations [10]. This ODE system offered the first glimpse of universal fractal scatterings in weak wave interactions, but these fractal patterns were not analyzed.

In this Letter, we analyze fractal-scattering patterns in weak solitary-wave interactions for generalized nonlinear Schrödiger equations. Using asymptotic methods, we reduce these weak interactions to a simple second-order map which contains no free parameters. It is shown that this universal map gives a complete characterization of fractal structures in these wave interactions. In addition, the scaling laws of these fractals for different initial conditions are analytically derived. These results provide a deep understanding of weak solitary-wave interactions for various physical applications.

The generalized nonlinear Schrödinger equations we consider in this Letter are

$$iU_t + U_{xx} + F(|U|^2)U = 0, \quad (1)$$

where $F(\cdot)$ is a general function. These equations govern various physical wave phenomena in nonlinear optics, fiber communications, and fluid dynamics [1–3]. This equation admits solitary waves of the form $U = \Phi(x - \xi)e^{i\phi}$, where $\Phi(\theta)$ is a localized positive function, $\xi = Vt + x_0$ is the wave's center position, and $\phi = \frac{1}{2}V(x - \xi) + (\beta + \frac{1}{4}V^2)t - \eta_0$ is the wave's phase. This wave has four free parameters: velocity V, amplitude parameter β, initial position x_0, and initial phase η_0. In weak interactions, two such solitary waves are initially well separated and have small relative velocities and amplitude differences. Then they would interfere with each other through tail overlapping. When time goes to infinity, they either separate from each other or form a bound state. The exit velocity, defined as $\Delta V_\infty = |V_2 - V_1|_{t\to\infty}$, depends on the initial conditions of the two waves.

To study weak interactions in Eq. (1), we select two different nonlinearities which are cubic-quintic and quadratic-cubic, respectively:

$$F(|U|^2) = |U|^2 + \gamma|U|^4, \quad F(|U|^2) = |U|^2 + \delta|U|. \quad (2)$$

Here γ and δ are real parameters. To illustrate results of weak interactions, we take $\gamma = 0.0003$ and $\delta = -0.0015$. The initial conditions are taken as

$$x_{0,1} = -x_{0,2} = -5, \quad V_{0,k} = 0, \quad \beta_{0,k} = 1 \quad (k = 1, 2), \quad (3)$$

$\phi_{0,1} = 0$, and the initial-phase difference $\Delta\phi_0 = \phi_{0,2} - \phi_{0,1}$ is used as the control parameter. In our numerical simulations of Eq. (1), the discrete Fourier transform is used to evaluate the spatial derivative ∂_{xx}, while the fourth-order Runge-Kutta method is used to advance in time. The exit velocity ΔV_∞ versus $\Delta\phi_0$ graphs for these two nonlinearities are plotted in Fig. 1. These graphs are fractals [10]. It is amazing that these fractals appear for such small values of γ and δ, where Eq. (1) is simply a weakly perturbed NLS equation. Notice that the fractals for these two different nonlinearities are very similar, signaling their universality in weak wave interactions.
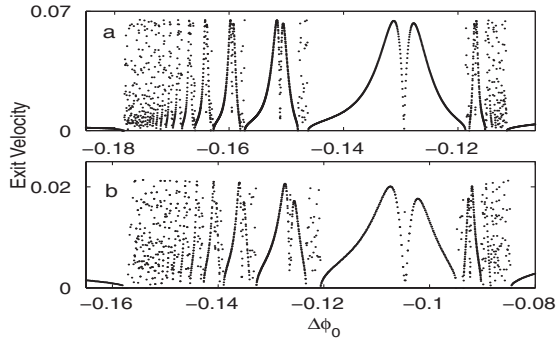
FIG. 1. Exit velocity versus initial-phase-difference graphs for initial conditions (3): (a) cubic-quintic nonlinearity; (b) quadratic-cubic nonlinearity.

To analyze this fractal-scattering phenomenon, the Karpman-Solov'ev method [4] was applied, and the following simple set of dynamical equations for solitary-wave parameters was derived [10]:

$$\zeta_{\tau\tau} = \cos\psi e^{\zeta}, \qquad \psi_{\tau\tau} = (1 + \varepsilon)\sin\psi e^{\zeta}. \qquad (4)$$

Here $\psi = \Delta\phi$, $\zeta = -\sqrt{\beta}\Delta\xi$,

$$\tau = \sqrt{16\beta^{3/2}c^2/P}t, \qquad \varepsilon = P/(2\beta P_\beta) - 1, \qquad (5)$$

$\Delta\xi$ and $\Delta\phi$ are the distance and phase difference between the two waves, $\beta = (\beta_{1,0} + \beta_{2,0})/2$, c is the tail coefficient of the solitary wave with propagation constant β, and $P(\beta)$ is the power function of the wave. These reduced ODEs capture fractal scatterings of weak wave interactions such as in Fig. 1 both qualitatively and quantitatively [10], and they represent an important first step toward the understanding of these phenomena. However, the fractal structures in the partial differential equations (PDEs) (1) and ODEs (4) have not been analyzed previously. Below we give a complete characterization for the first time of this fractal scattering by analyzing the ODEs (4).

If $\varepsilon = 0$, Eq. (4) is integrable. It has two conserved quantities, energy E and momentum M:

$$E = (\dot{\zeta}^2 - \dot{\psi}^2)/2 - e^{\zeta}\cos\psi, \qquad M = \dot{\zeta}\dot{\psi} - e^{\zeta}\sin\psi. \qquad (6)$$

Introducing two complex quantities

$$C = \sqrt{(E + iM)/2}, \qquad F = -\text{acoth}[(\dot{\zeta} + i\dot{\psi})/2C]/C, \qquad (7)$$

the analytical solution of Eq. (4) can be found to be

$$Y(\tau) = \ln[2C_0^2\text{csch}^2 C_0(\tau - \tau_0 + F_0)], \qquad (8)$$

where $Y = \zeta + i\psi$, and C_0, F_0 are the initial values of C and F. The third conserved quantity of Eq. (4) is $\text{Im}(F)$. Behaviors of the above integrable solutions should be noted. When $E > 0$, or $E \leq 0$ but $M \neq 0$, $\zeta \rightarrow -\infty$ (a degenerate saddle point) as $\tau \rightarrow \infty$, and thus these solutions are escape orbits. When $E < 0$ and $M = 0$, the orbits are periodic with period $T_p = \sqrt{2}\pi/\sqrt{|E|}$. Orbits with $E = M = 0$ separate the escape orbits from the periodic ones;

hence, we call them separatrix orbits. The formulas for separatrix orbits can be readily found to be

$$Y_s(\tau) = -\ln[\sigma A^{-1/2}i + (\tau - \tau_M)/\sqrt{2}]^2. \qquad (9)$$

Here $A = e^{\zeta_M}$, ζ_M is the maximum of $\zeta(\tau)$, τ_M is the time when $\zeta = \zeta_M$, and σ is the sign of $\dot{\psi}$ at $\tau = \tau_M$.

In the general case where $\varepsilon \neq 0$, Eq. (4) is still a Hamiltonian system with the conserved Hamiltonian

$$H(\zeta, \dot{\zeta}, \psi, \dot{\psi}) = E + \varepsilon\dot{\psi}^2/[2(1 + \varepsilon)], \qquad (10)$$

where E is given in Eq. (6). But E, M, and $\text{Im}(F)$ are not conserved anymore. In order to determine the fractal structures as shown in Fig. 1, we need to calculate the exit velocity, which corresponds to $|\dot{\zeta}_\infty|$ for Eq. (4). If the orbit has nonzero exit velocity, then from Eqs. (6) and (10), we find that

$$|\dot{\zeta}_\infty| = \sqrt{H + \sqrt{H^2 + M_\infty^2/(1 + \varepsilon)}}. \qquad (11)$$

Since H is conserved, to get $|\dot{\zeta}_\infty|$, we only need to find M_∞. For arbitrary values of ε, it is impossible to calculate M_∞ analytically. However, when $\varepsilon \ll 1$ as in Fig. 1 (where $\varepsilon = 0.001$ for both nonlinearities), the calculation of M_∞ can be done. In this case, Eq. (4) is weakly perturbed from the integrable case ($\varepsilon = 0$); thus, we will use asymptotic techniques in our calculations below.

To motivate our analysis, we first illustrate in Fig. 2(a) a typical ζ solution when the initial condition lies in the sensitive region of Fig. 1. We see that ζ undergoes several large oscillations, then escapes to $-\infty$. Each oscillation corresponds to a "bounce" in the two-wave interactions. These bouncing sequences are the key to the existence of fractal structures, similar to other physical systems [5–9]. Each local minimum of ζ will be called a saddle approach [11]. The corresponding $M(\tau)$ curve is also plotted in Fig. 2(a). We see that M changes very little near a saddle approach, but changes significantly near maxima of ζ. Below we will calculate the change in M from one saddle approach to another. It turns out the M formula will be coupled to E and F; thus, we need to calculate the changes
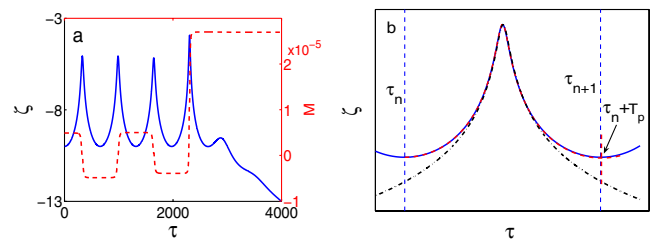

FIG. 2 (color online). (a) A typical ζ solution (blue or dark gray solid line) when $\Delta\phi_0$ is in the fractal region, and the corresponding $M(\tau)$ curve (red or gray dashed line); (b) plots of the perturbed solution $\zeta(\tau)$ (blue or dark gray solid line), the unperturbed solution (red or gray dashed line), as well as the separatrix solution (black dash-dotted line) from the nth saddle approach to the next.

in E, M, and F simultaneously. To carry out these calculations, we notice two facts. One is that from one saddle approach to the next, the perturbed and unperturbed (i.e., integrable) solutions remain close to each other since $\varepsilon \ll 1$. The other fact is that at each saddle approach, E_n, $M_n \ll 1$. This is so since initial E_0, M_0 are always small for weak wave interactions, and they will remain small when $\varepsilon \ll 1$. To simplify our analysis, we also assume that at each saddle approach, $M_n/E_n \ll 1$. This assumption is satisfied for many initial conditions such as (3).

Now we calculate E, M, and F from the nth saddle approach to the next. From Eqs. (4) and (6), we get

$$\Delta M_n = \int_{\tau_n}^{\tau_{n+1}} \frac{dM}{d\tau} d\tau = \int_{\tau_n}^{\tau_{n+1}} \varepsilon e^{\zeta} \sin\psi \dot{\zeta} d\tau. \quad (12)$$

In view of the first fact above, the perturbed orbit in the above formula can be approximated by the integrable orbit [see Fig. 2(b)]. Because of the second fact, we can further approximate the integrable orbit by a separatrix orbit. Notice that the separatrix orbit (9) has three parameters. To select the appropriate parameters in the separatrix, we note that most contributions to the integral of (12) come from the ζ-maximum region; thus, it is natural to ask the separatrix solution to have the same ζ-maximum point as the integrable solution [see Fig. 2(b)]. Then in view of Eq. (8), the above requirement selects σ and A in the separatrix (9) as

$$\sigma_n = \text{sgn}\{\text{Im}[-2C_n \coth(C_n(\tau_u^* + F_n))]\}; \quad (13)$$

$$A_n = 2|C_n^2 \text{csch}^2[C_n(\tau_u^* + F_n)]|. \quad (14)$$

Here $\tau_n + \tau_u^*$ is the time the unperturbed solution ζ_u reaches the maximum. Because of the assumption $M_n/E_n \ll 1$, the unperturbed solution (to leading order) is a periodic solution with period $T_p = \sqrt{2}\pi/\sqrt{|E_n|}$. Thus $\tau_u^* = T_p/2$ and $\tau_{n+1} = \tau_n + T_p$. Utilizing the above results and noticing $T_p \gg 1$, Eq. (12) is asymptotically approximated by

$$\Delta M_n = \varepsilon \int_{-\infty}^{+\infty} e^{\zeta_s} \sin\psi_s \dot{\zeta}_s d\tau = \sigma_n \varepsilon \pi A_n/2. \quad (15)$$

By similar calculations and using the symmetry properties of the separatrix solution (9), we find that

$$\Delta E_n = \varepsilon \int_{-\infty}^{+\infty} e^{\zeta_s} \sin\psi_s \dot{\psi}_s d\tau = 0. \quad (16)$$

To calculate F_{n+1}, notice from Eqs. (4) and (7) that F satisfies a linear inhomogeneous ODE:

$$\frac{dF}{d\tau} = -\frac{\dot{E} + i\dot{M}}{2(E + iM)} F + D, \quad (17)$$

where D is a function of (ζ, ψ) whose expression is easy to obtain. The homogeneous solution of this ODE is $C^{-1}(\tau)$. Thus by using the method of variation of parameters, we can integrate the inhomogeneous ODE (17) from τ_n to τ_{n+1} and get

$$F_{n+1} = F_n \frac{C_n}{C_{n+1}} + \frac{\int_{\tau_n}^{\tau_{n+1}} \sqrt{E + iM} D d\tau}{\sqrt{E_{n+1} + iM_{n+1}}}. \quad (18)$$

Because of the second fact of E_n, $M_n \ll 1$, we can approximate the solution (ζ, ψ) in D by the separatrix solution (9). Then to leading order in ε, we get

$$F_{n+1} = F_n \frac{C_n}{C_{n+1}} + \frac{(\hat{\tau} + i\alpha)\sqrt{E + iM}|_{\tau_n}^{\tau_{n+1}}}{\sqrt{E_{n+1} + iM_{n+1}}}. \quad (19)$$

Here $\hat{\tau} = \tau - \tau_n - T_p/2$, and $\alpha = \sqrt{2}\sigma_n A_n^{-1/2}$.

Iteration Eq. (19) is quite complicated. Below, we simplify it. From Eq. (16), we get $E_n = E_0$. Under our assumption of $M_n/E_n \ll 1$, to leading order, Eq. (19) becomes

$$F_{n+1} = \frac{\pi}{\sqrt{2|E_0|}} + \left(F_n + \frac{\pi}{\sqrt{2|E_0|}}\right)\left(1 - \frac{M_{n+1} - M_n}{2E_0}i\right). \quad (20)$$

At the initial saddle approach, we find from Eq. (7) that $\text{Re}(F_0) = -\pi/\sqrt{2|E_0|}$. Then solving Eq. (20), we get

$$F_n = \pi(2|E_0|)^{-1/2}[2n - 1 - iS_nM_n/2E_0], \quad (21)$$

where $S_{n+1}M_{n+1} = 2nM_{n+1} - (2n - S_n)M_n$. Now we introduce a new variable Q_n:

$$Q_n - 2nM_n = -S_nM_n = -(2|E_0|)^{3/2}\text{Im}[F_n]/\pi. \quad (22)$$

Then substituting formula (21) into (13) and (14), keeping only their leading order terms in M_n/E_n, and putting the resulting expressions into (15), we obtain the simplified iteration equations as

$$M_{n+1} = M_n - \text{sgn}(Q_n)8|E_0|^3\varepsilon/\pi Q_n^2, \quad (23)$$

$$Q_{n+1} = Q_n + 2M_{n+1}. \quad (24)$$

These equations are derived asymptotically near the separatrix orbit (9), and will be called the separatrix map. This map can be further normalized. Let

$$G = 8|E_0|^3\varepsilon/\pi, \qquad \tilde{M}_n = G^{-1/3}M_n, \quad (25)$$
$$\tilde{Q}_n = G^{-1/3}Q_n,$$

then the normalized separatrix map is

$$\tilde{M}_{n+1} = \tilde{M}_n - \frac{\text{sgn}(\varepsilon\tilde{Q}_n)}{\tilde{Q}_n^2}, \quad (26)$$

$$\tilde{Q}_{n+1} = \tilde{Q}_n + 2\tilde{M}_{n+1}. \quad (27)$$

This is a simple but important second-order area-preserving map, and it does not have any parameters in it (except a sign of ε). This *universal* map governs weak two-wave interactions in generalized NLS equations (1).

Now we compare this map's predictions with direct PDE simulations. Here we take the cubic-quintic nonlinearity in (2) with γ and initial conditions as for Fig. 1(a). For the
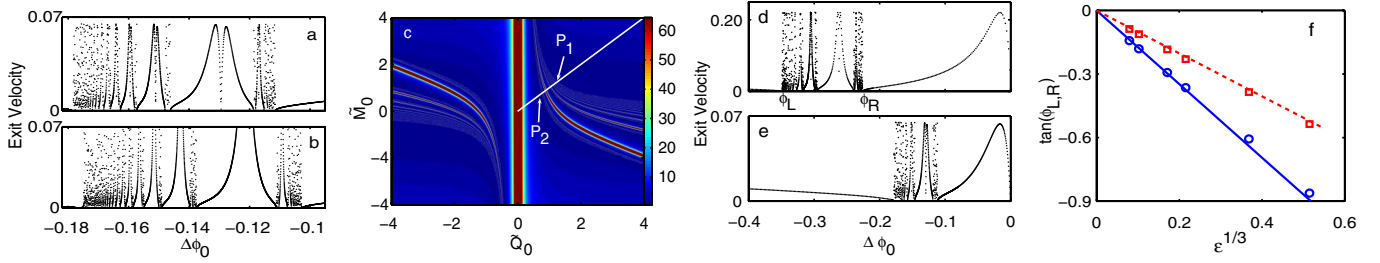
FIG. 3 (color online). (a),(b) The exit-velocity versus initial-phase-difference graphs from (a) PDE simulations and (b) map predictions; (c) the map's $|\tilde{M}_\infty|$ graph in the $(\tilde{Q}_0, \tilde{M}_0)$ plane; (d),(e) exit-velocity versus initial-phase-difference graphs of the PDE for $\varepsilon = 0.01$ and 0.001, respectively; (f) plots of the accumulation points ϕ_L and ϕ_R versus ε from PDE simulations (circles and squares) and map predictions (solid and dashed lines).

map, we iterate it to infinity to get $\tilde{M}_\infty$ (in practice, 500 iterations performed), which in turn gives $|\dot{\zeta}_\infty|$ from formula (11). With the variable scalings (5) and (25) considered, the exit velocity graph predicted from the map (26) and (27) is shown in Fig. 3(b), while that from the PDE simulations is shown in Fig. 3(a). Comparing these two graphs, it is clear that the map gives a good replication of the PDE's fractal structure both qualitatively and quantitatively.

The separatrix map (26) and (27) exhibits a fractal structure in the graph of $|\tilde{M}_\infty|$ as a function of initial values $(\tilde{Q}_0, \tilde{M}_0)$, which is displayed in Fig. 3(c) [with sgn(ε) = 1]. This fractal of the map completely determines the fractal structures in the PDEs (1). For instance, for initial conditions (3), the corresponding initial values of the map are

$$\tilde{Q}_0 = \tilde{M}_0 = -2^{-1}(\pi/\varepsilon)^{1/3}\tan(\Delta\phi_0). \qquad (28)$$

As $\Delta\phi_0$ varies, Eq. (28) gives a parametrized curve in the $(\tilde{Q}_0, \tilde{M}_0)$ plane, which is the white straight line in Fig. 3(c). This line cuts across the fractal of the map in Fig. 3(c), and the intersection is precisely the fractal structure as observed in Fig. 1 for the PDE [see also Figs. 3(a) and 3(b)]. The scaling laws for fractals of the PDEs can be readily derived from Eq. (28) and Fig. 3(c). Let P_1 and P_2 denote the two accumulation points of the map's fractal, which are $(\tilde{Q}_0, \tilde{M}_0) = (1.271, 1.271)$ and $(0.741, 0.741)$ as marked in Fig. 3(c). The corresponding accumulation points ϕ_R and ϕ_L in the fractal structures of the PDEs are marked in Fig. 3(d). Here ϕ_L and ϕ_R are the left and right ends of the fractal region. Then according to scalings (28), we find that $\phi_R = -\text{atan}(1.482\varepsilon^{1/3}/\pi^{1/3})$ and $\phi_L = -\text{atan}(2.542\varepsilon^{1/3}/\pi^{1/3})$. Hence the map analytically predicts that the fractal region of the PDE shrinks to $\Delta\phi_0 = 0$ as $\varepsilon \to 0$, and its shrinking speed is proportional to $\varepsilon^{1/3}$ for $\varepsilon \ll 1$. This is precisely what happens. To illustrate, we choose two γ values 0.0029 and 0.0003 in Eq. (2), which correspond to $\varepsilon = 0.01$ and 0.001, respectively. The fractal structures of the PDEs for these γ values are displayed in Figs. 3(d) and 3(e). It is seen that the fractal region indeed shrinks as ε decreases. We further recorded the ϕ_L and ϕ_R

values in the PDE fractals at a number of ε values, and the data are plotted in Fig. 3(f). The theoretical formulas of ϕ_L and ϕ_R above are also plotted for comparison. It is seen that the PDE values and the map's analytical predictions agree perfectly, confirming the asymptotic accuracy of the map (26) and (27).

In summary, we have asymptotically analyzed weak solitary-wave interactions in the generalized nonlinear Schrödinger equations and obtained a simple universal map. This map gives a complete analytical characterization of universal fractal structures in these wave interactions. We expect that this work will stimulate research in other physical systems where weak solitary-wave interactions arise, such as nonlinear optics, water waves, and Bose-Einstein condensates.

[1] M. J. Ablowitz and H. Segur, *Solitons and the Inverse Scattering Transform* (SIAM, Philadelphia, 1981).

[2] A. Hasegawa and Y. Kodama, *Solitons in Optical Communications* (Clarendon, Oxford, 1995).

[3] Y. Kivshar and G. Agrawal, *Optical Solitons* (Academic Press, San Diego, 2003).

[4] V. I. Karpman and V. V. Solov'ev, Physica (Amsterdam) **3D**, 142 (1981); K. A. Gorshkov and L. A. Ostrovsky, Physica (Amsterdam) **3D**, 428 (1981).

[5] D. K. Campbell, J. S. Schonfeld, and C. A. Wingate, Physica (Amsterdam) **9D**, 1 (1983); M. Peyrard and D. K. Campbell, Physica (Amsterdam) **9D**, 33 (1983).

[6] P. Anninos, S. Oliveira, and R. A. Matzner, Phys. Rev. D **44**, 1147 (1991).

[7] Y. S. Kivshar, Z. Fei, and L. Vázquez, Phys. Rev. Lett. **67**, 1177 (1991); Zhang Fei, Y. S. Kivshar, and L. Váquez, Phys. Rev. A **45**, 6019 (1992).

[8] J. Yang and Y. Tan, Phys. Rev. Lett. **85**, 3624 (2000); Y. Tan and J. Yang, Phys. Rev. E **64**, 056616 (2001).

[9] S. V. Dmitriev, Yu. S. Kivshar, and T. Shigenari, Phys. Rev. E **64**, 056613 (2001); S. V. Dmitriev and T. Shigenari, Chaos **12**, 324 (2002).

[10] Y. Zhu and J. Yang, Phys. Rev. E, **75**, 036605 (2007).

[11] R. H. Goodman and R. Haberman, SIAM J. Appl. Dyn. Syst. **4**, 1195 (2005); R. H. Goodman and R. Haberman, Phys. Rev. Lett. **98**, 104103 (2007).